

# AA241X Final Report

Apoorva Sharma, Justin Schneider, Miao Zhang, Victoria M Dax, Zhe Zhang and Zhengyu Huang

June 13, 2017



## Contents

<b>I</b>	<b>Aircraft Design</b>	<b>2</b>
I.1	Theoretical Analysis and Design . . . . .	2
I.1.1	Matching Earth and Mars Flight Conditions . . . . .	2
I.1.2	Lift, Moment and Longitudinal Stability . . . . .	2
I.1.3	Calculation of Lift from Data . . . . .	4
I.1.4	Fuselage Drag . . . . .	4
I.1.5	Thrust, Drag and Power Required . . . . .	6
I.1.6	Climb . . . . .	6
I.1.7	Propulsive model . . . . .	7
I.1.8	Wing Design . . . . .	9
I.1.9	Flight dynamics . . . . .	16
I.2	Manufacturing . . . . .	18
<b>II</b>	<b>Controls and Planning</b>	<b>22</b>
II.1	Low Level Control System Design . . . . .	23
II.1.1	Longitudinal Autopilot . . . . .	23
II.1.2	Lateral Autopilot . . . . .	24
II.1.3	Control Parameters . . . . .	25
II.2	Path Planning . . . . .	25
<b>III</b>	<b>Results and Analysis</b>	<b>26</b>
III.1	Bixler Mission Test . . . . .	26
III.2	Albatross Mission Test . . . . .	27

## I Aircraft Design

### I.1 Theoretical Analysis and Design

#### I.1.1 Matching Earth and Mars Flight Conditions

Since we need to match the dynamical scaling of actual Mars airplane, it is necessary to discuss about the Mars conditions and make some calculations.

The temperature on Mars varies from  $-153^{\circ}C$  at the poles to  $20^{\circ}C$  at noon at the equator. By using a common value of  $-55^{\circ}C$ , and approximate the atmosphere as 100% $CO_2$  instead of 95% $CO_2$  (to simplify calculation), we can get the dynamic viscosity of  $\mu = 1.106 \times 10^{-5} kg/(m \cdot s)$ . Dividing it by the density, we can get the kinematic viscosity of  $\nu = 8.851 \times 10^{-4} m^2/s$ . For viscosity in other conditions, we can use this online calculator (<http://www.lmnoeng.com/Flow/GasViscosity.php>)

The gas constant for  $CO_2$  is  $R_{CO_2} = 188.9 J/(kg \cdot K)$ , the ratio of specific heats for  $CO_2$  is  $\gamma_{CO_2} = 1.28$ . An estimate of speed of sound on Mars using is:  $a = \sqrt{\gamma RT} = 229.667 m/s$

To match the Mars airplane parameters, the chord length  $c$ , velocity  $u$  and mass  $m$  should satisfy the relations

$$\frac{m}{c^3} = 658.20586 \quad \frac{m}{u^2 c^2} = 0.3564957 \quad \frac{c}{u^2} = 0.000542$$

Given the flight speed range, we can estimate the range of wing chord length:

$$\begin{array}{lll} u = 15 m/s & c = 0.1219 m & Re = \frac{\rho c u}{\mu} = 1.23 \times 10^5 \\ u = 20 m/s & c = 0.216646 m & Re = \frac{\rho c u}{\mu} = 2.9 \times 10^5 \end{array}$$

From this range, and the NASA ARES Aircraft Characteristics 7, we can come up with approximate sizing of our plane.

#### I.1.2 Lift, Moment and Longitudinal Stability

Lift and Moment are closely related through shape and size of the plane. They together directly affect the static longitudinal stability of the plane.

An aircraft with throttle off, must produce a sufficient pitching moment to counter any perturbation in pitch, and the following inequality is a criterion:

$$\frac{\partial C_{M_{C.G.}}}{\partial \alpha} < 0$$

Considering about the center of gravity:

$$\frac{\partial C_{M_{C.G.}}}{\partial \alpha} = -C_{L_{\alpha w}} \frac{x_{acw} - x_{cg}}{\bar{c}} + C_{M_{\alpha f}} - \eta_h C_{L_{\alpha h}} \left(1 - \frac{d\varepsilon}{d\alpha}\right) \frac{S_h}{S_w} \frac{x_{ach} - x_{cg}}{\bar{c}},$$

where:

$C_{L_{\alpha w}}$  is the wing lift curve slope;

$C_{L_{\alpha h}}$  is the horizontal tail lift curve slope;

$S_w$  and  $S_h$  are areas of wing and tail respectively;

$\bar{c}$  is the mean aerodynamic chord defined as

$$\bar{c} = \frac{2}{S} \int_0^{\frac{b}{2}} c^2 dy$$

where  $b$  is the span,  $y$  is the coordinate along the wing span and  $c$  is the chord at the coordinate  $y$ .

The pitching moment generated by the fuselage ( $C_{M_{\alpha f}}$ ) can be found from NACA report 711 (<http://naca.central.cranfield.ac.uk/reports/1941/naca-report-711.pdf>) using the empirical data.

By calculation, Bixler 3 was found to have:

$$\frac{\partial C_{M_{C.G.}}}{\partial \alpha} = -1.0807 < 0,$$

which agrees with the fact that it is very stable. This tells us that, if we design a plane that has a similar configuration to the Bixler 3, we are likely to achieve good stability.

Another important concept that can be derived from the discussion above, is the neutral point, i.e. the C.G. position that would not result in a pitching moment with changing angle of attack (aircraft's aerodynamic center). It is given by:

$$\frac{x_{np}}{\bar{c}} = \frac{C_{L_{\alpha w}} \frac{x_{acw}}{\bar{c}} - C_{M_{\alpha f}} + \eta_h C_{L_{\alpha h}} \left(1 - \frac{d\varepsilon}{d\alpha}\right) \frac{S_h}{S_w} \frac{x_{ach}}{\bar{c}}}{C_{L_{\alpha w}} + \eta_h C_{L_{\alpha h}} \left(1 - \frac{d\varepsilon}{d\alpha}\right) \frac{S_h}{S_w}}$$

The aircraft's aerodynamic center ( $x_{np}$ ) must be aft of the aft most C.G. position to ensure static stability, this gives us a way of quick test for static stability.

Again, by calculation, the neutral point of Bixler 3 is found to be  $x_{np} = 0.3545[m]$ , which is slightly aft of the C.G. ( $x_{cg} = 0.32[m]$ ).

### I.1.3 Calculation of Lift from Data

To calculate the maximum lift coefficient, we first solved for the lift and drag of the aircraft. The Pixhawk took an enormous amount of data from our flight test so to simplify the amount of data processing, only data with no throttle input and a roll angle between  $\pm 3$  degrees was used. Then a free-body diagram was drawn with both the wind and body axes present as well as the lift, drag, and weight forces.

The summation of forces was then taken in both the x and z directions.

$$ma_x = L \sin \alpha - W \sin \alpha - D \cos \alpha$$

$$ma_z = L \cos \alpha + D \sin \alpha - W \cos \alpha$$

This gives two equations for the two unknowns L and D. The angle of attack  $\alpha$  is the z velocity component divided by the u velocity component and  $a_x$  and  $a_z$  are the body axis accelerations in the x and z directions. Because the accelerometer is raw, the gravity component was subtracted from each body axis acceleration based on the pitch angle.

$$a_{x_{new}} = a_x + g * \sin \alpha$$

$$a_{z_{new}} = a_z - g * \cos \alpha$$

Once these body axis accelerations were corrected, a simple matrix inversion can solve for the lift and drag for each point given mass, weight, pitch angle, and acceleration.

### I.1.4 Fuselage Drag

Fuselage drag usually lies in the range of 30  $\sim$  50% of the total zero-lift drag of the airplane. A more accurate estimation has to do with the fineness ratio  $l_B/d$ , where  $l_B$  is the length of the fuselage, and  $d$  is the max diameter of the fuselage. The fineness ratio for our plane is  $l_B/d \approx 49/7.4 \approx 6.6$ . According to the book “*Airplane Aerodynamics and Performance*” by Jan Roskam and C.T.Lan, a formula for the estimated fuselage zero-lift drag coefficient is given by:

$$C_{D_{0f}} = R_{wf} C_{ff} \left[ 1 + \frac{60}{(l_B/d)^3} + 0.0025 \left( \frac{l_B}{d} \right) \right] \frac{S_{wetf}}{S_{wing}}, \quad (1)$$

where  $R_{wf}$  is the wing-fuselage interference factor shown in the figure I.1.4;

$S_{wetf}$  is the wetted area of the fuselage;  $C_{ff}$  is the turbulent flat plane skin-friction coefficient

of the fuselage given by

$$C_{ff} = \frac{0.455}{(\log_{10} R_N)^{2.58} (1 + 0.144 M^2)^{0.58}}$$

The fuselage Reynolds number is defined as:

$$R_N = \frac{\rho U l_f}{\mu}$$

During our flight test, the speed range is about  $15 \sim 20$  m/s, by choosing  $\rho = 1.225$  kg/m<sup>3</sup>,  $\mu = 1.81 \times 10^{-5}$  kg/m/s, the corresponding  $R_N$  value is about  $497445 \sim 663260$ . Since the plot below is starting from  $10^6$ , we can make a guess that the  $S_{wetf}$  value could be around 1.0. The speed of sound is about  $\sqrt{1.4 \times 287 \times 298.15} = 346$  m/s, and the Mach number is in the range of  $0.043 \sim 0.058$ . By plugging in all the values, the fuselage zero-lift drag coefficient is about  $0.0081 \sim 0.0085$ . In the normal, take-off, cruise and landing angle of attack range, the fuselage drag coefficient due to lift tends to be quite negligible, so if we choose the average of the lower and upper bounds we calculated, the estimated overall fuselage drag coefficient is 0.0083.

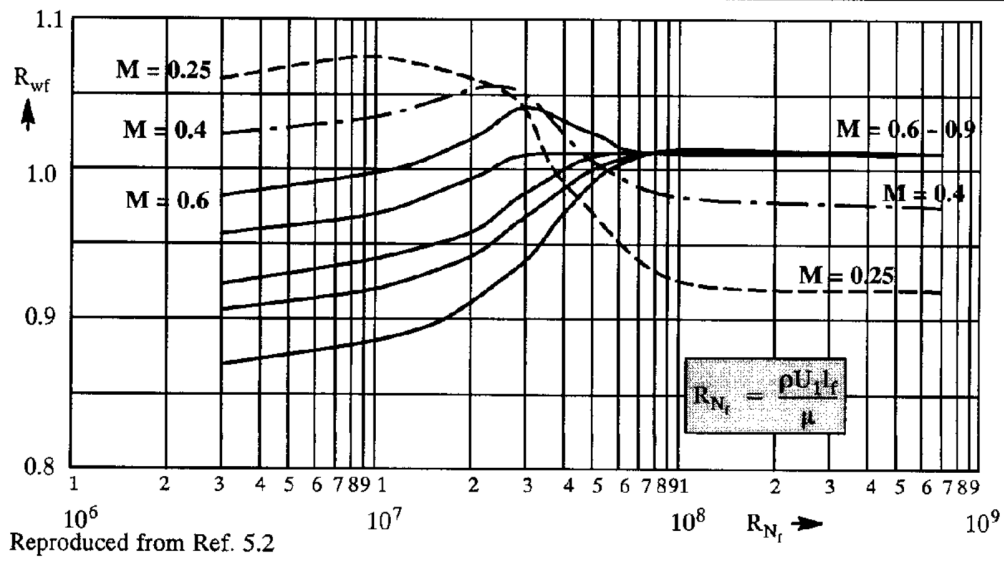


Figure 1: Wing Fuselage Interference Factor

### I.1.5 Thrust, Drag and Power Required

Thrust and Drag are closely related, and their relative size determines the power required. For level flight, the power required for level flight is just the power to overcome drag:

$$P_{\text{required}} = DV = \frac{1}{2}\rho C_{D_0} V^3 S + \frac{W^2}{\frac{1}{2}\rho V S} \left( \frac{1}{\pi e \mathcal{R}} \right)$$

The velocity for minimum power is:

$$V_{\text{min power}} = \left[ \frac{4}{3} \left( \frac{W}{S} \right)^2 \frac{1}{\rho^2} \frac{1}{C_{D_0}} \left( \frac{1}{\pi e \mathcal{R}} \right) \right]^{\frac{1}{4}}$$

For our Albatross, the theoretical drag coefficient without fuselage is calculated to be 0.069 using XFLR5, and from the previous part, the fuselage drag coefficient is about 0.0083 (choosing the average of the bounds), so the overall  $C_d = 0.0773$ .

### I.1.6 Climb

Given altitude  $h$  and velocity  $V$  of the aircraft, the energy is given by:

$$\varepsilon = \frac{1}{2}mV^2 + mgh,$$

from which the specific energy is:

$$h_e = \frac{\varepsilon}{mg} = \frac{V^2}{2g} + h,$$

For a climbing aircraft, the following relation holds:

$$m\dot{V} = T - D - mg \sin \gamma,$$

and the rate of climb is given by

$$\dot{h} = V \sin \gamma.$$

The rate of change of specific energy is:

$$\dot{h}_e = \frac{V}{g} \dot{V} + \dot{h} = \frac{V(T - D)}{mg}.$$

The ability of the aircraft to climb or accelerate, depends on the specific excess power,  $P_s$ . It has to be equal to the rate of change of specific energy:

$$P_s = P_{\text{available}} - P_{\text{required}} = \dot{h}_e = \frac{V(T - D)}{mg}.$$

The minimum time to climb is given by:

$$t_2 - t_1 = \int_{h_{e1}}^{h_{e2}} \frac{dh_e}{P_s},$$

where subscripts '1' and '2' refer to initial and final times respectively. Let  $\gamma$  be the climb angle, the power required is

$$P_{\text{required}} = (D + \cos \gamma mg)V = \frac{1}{2}\rho C_d V^3 S + \cos \gamma mgV$$

### I.1.7 Propulsive model

The motor for Albatross is Turnigy D2836/9 950KV Brushless Outrunner Motor, the no load current is  $i_0 = 1A$  and internal resistance is  $R = 0.070\Omega$ . and the RPM is 950Kv. We can compute motor speed constant as

$$Kv = \frac{950}{1V_{olt} - i_0 R} = 1021.50 \frac{rpm}{V_{olt}}$$

The motor for Bixler3 is 2620-1400kv Brushless Outrunner, the no load current is  $i_0 = 1A$  and internal resistance is  $R = 0.070\Omega$ . and the RPM is 1400Kv. We can compute motor speed constant as

$$Kv = \frac{1400}{1V_{olt} - i_0 R} = 1505.38 \frac{Rpm}{V_{olt}}$$

The torque power, efficiency vs. rotation rate are computed as

$$\begin{aligned} Q_m(\Omega, v) &= \left[ \left( v - \frac{\Omega}{K_v} \right) \frac{1}{R} - i_0 \right] \frac{1}{K_v} \\ P_{\text{shaft}}(\Omega, v) &= \left[ \left( v - \frac{\Omega}{K_v} \right) \frac{\Omega}{R} - i_0 \right] \frac{1}{K_v} \\ \eta_m(\Omega, v) &= \left[ 1 - \frac{i_0 R}{v - \Omega/K_v} \right] \frac{\Omega}{v K_v} \end{aligned}$$

and showed in Fig 2 3 4

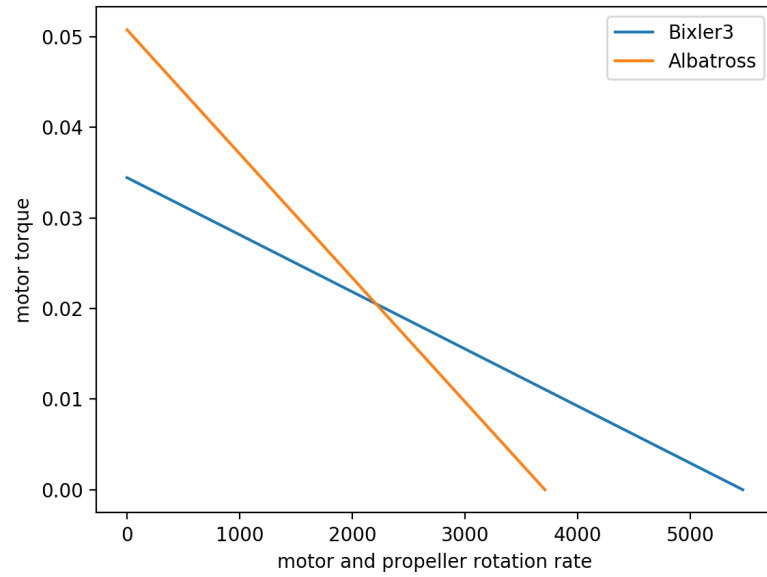


**Figure 2:** Torque vs. rotation rate at  $V=12\text{V}$

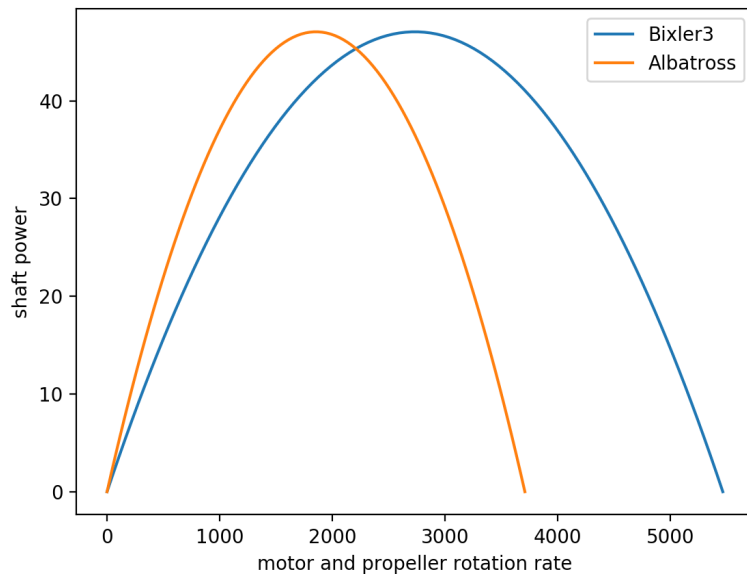


**Figure 3:** Power vs. rotation rate at  $V=12\text{V}$



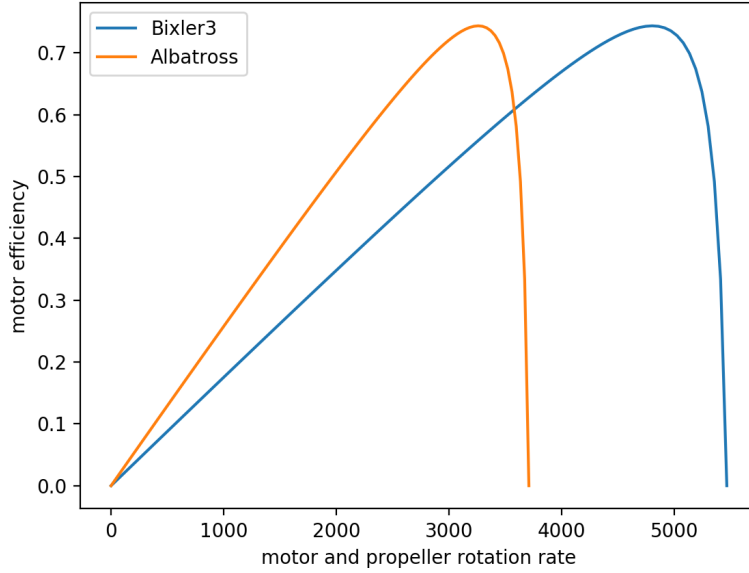


**Figure 4:** Efficiency vs. rotation rate at  $V=12\text{V}$

The motor for Albatross has lower rotation rate compared with that of Bixler3. The motor of Albatross is most efficient at rotation rate about 10000 rpm, and the motor of Bixler3's motor reaches maximum efficiency at 16000 rpm.

### I.1.8 Wing Design

Ultimately, the goal was to design a fixed wing airplane that would be able to accomplish a given mission in minimum time.

The mission of our aircraft is to maximize the number of visited sites, plumes in a two-dimensional plane, in autonomous flight during a limited communication window of 90 seconds total. The mission was inspired by discussions to use robotic aircrafts for Mars exploration. As this idea has been studied by NASA, dimensionless parameters of our plane design has to match the *Mars ARES project* ones, which had a similar mission.

The important aerodynamic parameters are Reynolds number, Mach number, lift coefficient, AR and dimensionless mass, which are summarized in the table 7

**Table 1:** NASA ARES Aircraft Characteristics

Mass (kg)	2.3
Span (m)	4.2
Aspect Ratio	6.0
Cruise Velocity ( $\frac{m}{s}$ )	22.0
Atmospheric Density ( $\frac{kg}{m^3}$ )	0.15
Speed of Sound ( $\frac{m}{s}$ )	225
Gravitational Acceleration ( $\frac{m}{s^2}$ )	3.7

*Due to the constraints on dimensionless mass and  $C_l$  we expect required cruise velocities that are very close to stalling speeds. This is very likely to make design and control implementation difficult.*

Let's consider the most important parameters independently.

First, the Reynolds number for any aircraft on Mars is going to be very low. The Reynolds number of the ARES aircraft was calculated to be about 60,000, which is almost impossible for us to simulate on Earth without flying at extremely high altitudes.

Fortunately, compressibility boundary layer effects can be neglected for lower speeds, which implies that as long the Mach number is below .3 we can fly at a different Re number. We expect to be flying at Mach .05 which is well below the upper limit for compressibility effects to occur.

Next, the lift coefficient is one of the parameters that we will try to match exactly. Using the equation for lift coefficient  $C_L = \frac{L}{\frac{1}{2}\rho V^2 S_w}$ , our lift coefficient will be 0.80 at cruise condition.

Finally, the non-dimensional mass of the ARES has to be matched, it will affect many aspects of the aircraft handling, such as damping and stability modes. The equation for non-dimensional mass is  $\mu_s = \frac{m}{\rho S_w c}$ , which is equal to 74.5 for ARES.

Because performing well in our mission depends on how many plumes can be reached within the allotted time, we decided a high cruising velocity was critical. However, due to the lift coefficient and non-dimensional mass matching, the mass of our plane increased dis-proportionally with an increase in cruise velocity. Figure ?? depicts the relation between

mass (on Earth), span width and chord length and cruise velocity under the outlined design constraints.

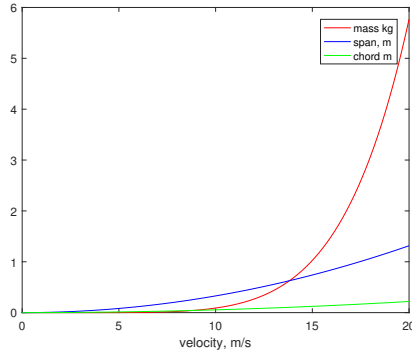


**Figure 5:** Design Parameters over Cruise Velocity

Note that, setting cruise velocity will define chord, span and wing area accordingly.

**Weight Breakdown** Before we get started on the layout we would have to make a preliminary weight estimation based on fuselage, wing area and material density, battery, propulsion system, motors and required software. As for Table 2 is the detailed list of components for further reference.

**Table 2:** Weight break-down [g]

Total preflight mass	940
Fuselage	199
Battery	177
Wing + Aileron + Servos	106
Wing box	99
Electronics	58
Tail assembly + rod	65

**Airfoil Design** Let our first design point be the airfoil shape. Due to the high velocities that we would like to yield we expect a the requirement of high  $C_{l_{max}}$ . The maximum lift coefficient determines the maximum roll angles, and the level flight stall velocity. Unfortunately even with a  $C_{l_{max}}$  of 1.6 - a generous and optimistic estimation - we would estimate stall velocities of about 11 m/s depending on the wing design and mass of the plane. Hence high  $C_{l_{max}}$  will be critical at take-off and landing.

On the other side, we estimate the drag coefficient to be of no critical importance, since we are not power limited during flight. Clearly lower drag coefficient are preferable, but they will not be considered pivotal for decision making.

Using XFLR5, we were able to simulate the performance and identify important characteristics of well-known airfoil shapes: FX 63-137 Sm Airfoil (Figure ??), FX 74-CL5-140 MOD Airfoil, S1210 Airfoil and S1223 Airfoil.

As a result of this analysis, we were able see the outstanding performance of the S1223 airfoil. But, for reasons of structural stability and stable flight characteristics, we opted for the FX 63-137-smoothed shape, which has less chamber and is thicker compared to the s1223 airfoil.

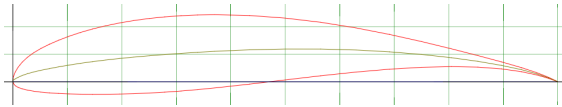


**Figure 6:** FX 63-137 Sm Airfoil

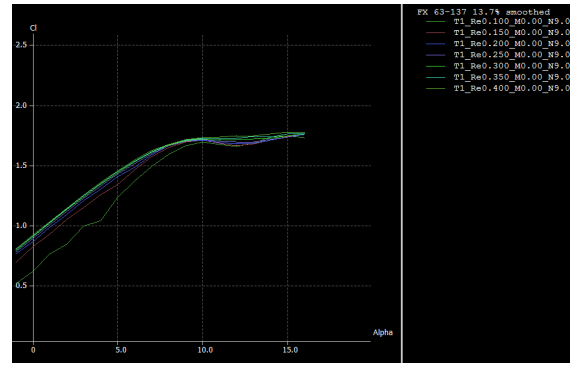


**Figure 7:** Cl vs Alpha

**Iteration 1** For our first wing design we set the cruise velocity to 16  $m/s$  which led to the design of a rather large and heavy 1.51 kg plane, requiring additional .6 kg in order to meet the dynamic scaling requirements.

A summary of our aircraft specifications is shown below.

**Table 3:** Albatross Aircraft Parameters

Mass (kg)	1.512
Span (m)	0.842
Aspect Ratio	6.0
Cruise Velocity ( $\frac{m}{s}$ )	16.0
Wing Area ( $m^2$ )	0.118
Chord (m)	0.14

Using these parameters and the previously defined airfoil shape we were now able to run full 3D wing analysis with XFLR5 and iterate until high maximum  $C_l$  were found with a

configuration that met the requirements. Ultimately we found a  $C_{l_{max}}$  of 1.67 with a  $C_D$  of 0.61 with the design depicted in Figure ?? . Next, the tail had to be designed. The main goal for its layout was to achieve stability in all main modes including short, phugoid, roll, dutch roll and spiral mode. However, the main issue was that we were not able to stabilize the spiral mode: from literature though we knew that this was not uncommon and as will be outlined in section (ref) the control implementation was not too convoluted to be taken care of.

Please refer to table 6 for a full description of the wing configuration.

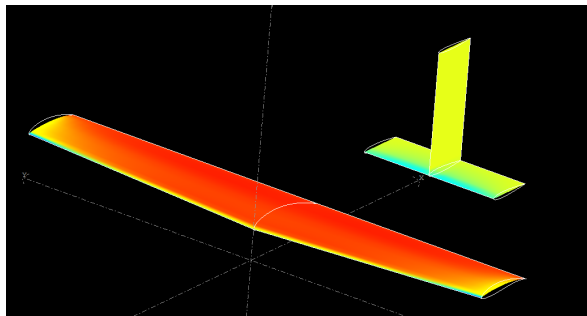


**Figure 8:** Plane Design in XFLR5

**Flight Testing** These first flight tests with our self-build plane were to investigate general dynamic behavior and eventually setting some trim preferences. We were able to successfully take off, but crashed twice due to improper trimming. Unfortunately on the third test our wing collapsed during a pull-up maneuver. As a consequence, one main design improvement for Albatross 2.0 was to reinforce the structure of the main wing.

**Iteration 2** For our second iteration, i.e. Albatross 2.0, we wanted to address majorly the following three concerns:

1. Weight. We laid the first airplane out for a mass of 1.5 kg but flew it at 1.2 kg.
2. Construction. We did not have a continuous spar throughout the entire main wing, making it susceptible to fail in this region since great aerodynamic forces apply in this region.
3. As a stretch goal we are considering stabilizing the phugoid mode.

We addressed the first issue at the very beginning of the redesigning phase. Setting the goal weight to the feasible minimum, as it can be taken out of Table 2, we were aiming for

940g, which set the cruise velocity respectively to 14.5 m/s. The other design parameters were then to be accordingly:

**Table 4:** Albatross Aircraft Parameters

Mass (kg)	0.940
Span (m)	0.71
Aspect Ratio	6.0
Cruise Velocity ( $\frac{m}{s}$ )	14.5
Wing Area ( $m^2$ )	0.084
Chord (m)	0.12

The other two design issues that were previously mentioned were solved by running an XFLR5 3D wing analysis for various shapes and lay-outs. Note that we were using the same airfoil as for our first plane iteration. The final design we decided to manufacture is depicted in Figure ??.

It the continuous midsection allows us to foam-cut the piece as one part and hence enables to use one spar throughout this section, reinforcing the part that failed at our last test flights. It has also been the configuration that was moving the spiral mode poles farthest towards the origin, but still not stabilizing them entirely. Please refer to table 6 for a full description of the wing configuration and a comparison to our first iteration.

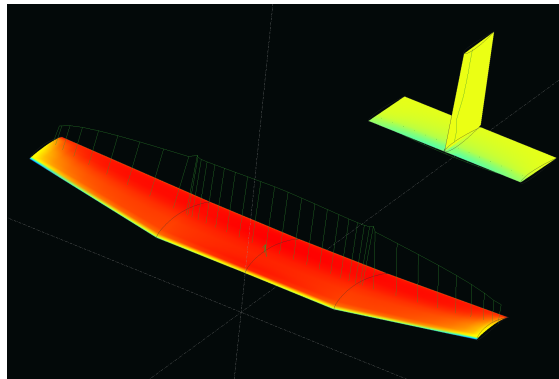


**Figure 9:** Plane Design in XFLR5

**Flight Testing** When we test flew this plane, we were able to see the considerable difference to our first design. Due to its light weight, that ended up being of 980g, take-off had to be against the wind and required to even throw it a little to yield higher velocities. Other than that the we were able to fly manually until the control gains were tuned and we use the

design for control testing. Our pilot explained that the plane had the tendency to induce rolling to the right, which we thought might be caused by an unsymmetrical manufacturing. But the controller was able to compensate for the deviations.

Unfortunately we broke some of our planes' parts during initial flights, when testing the line following and altitude hold. We manufactured them and put the plane back together. Ultimately, on our last test flight, we had issues during take off when implemented gain on the ailerons was of the opposite sign which reinforced the bank angle instead of recovering and stabilizing the UAV. The plane nosedived pretty quickly after a few meters due to a high roll angle that our pilot could unfortunately recovered in the too short period of time.

Consequently, to address the unstable wing lay-out, we are going to redesign the wing in a much simpler way such that these manufacturing artifacts do not impede the success of our total operating system.

**Iteration 3** Please refer to table 6 for a full description of the wing configuration.

**Table 5:** Albatross Aircraft Parameters

Mass (kg)	.990
Span (m)	0.80
Aspect Ratio	6.0
Cruise Velocity ( $\frac{m}{s}$ )	14.8
Wing Area ( $m^2$ )	0.084
Chord (m)	0.13

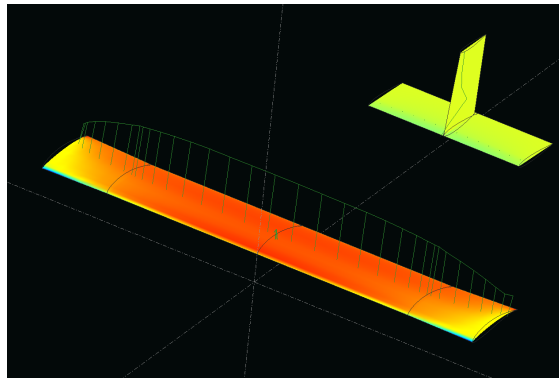


**Figure 10:** Plane Design in XFLR5

**Flight Testing** Please refer to Section III. for our ultimate results and their analysis.

**Table 6:** Albatross Wing Configuration

	I1	I2	I3
Wing Area ( $m^2$ )	0.118	.084	.106
Dihedral (deg)	3.0	8.5	0.0
Wing Twist (deg)	-1.0	-2.0	-3.0
Root Chord (m)	0.165	.135	1.33
Tip Chord (m)	0.115	.08	1.33
Mean Aerodynamic Chord (m)	0.141	.12	.13
Half-Span (m)	0.421	.350	.4
Root-Tip Sweep (deg)	-1.701	-.12	0.00
Aspect Ratio	6.01	6.00	6.02
Distance from Wing LE to Tail LE (m)	0.45	.5	.55
Horizontal Tail Span (m)	0.24	.24	.28
Horizontal Tail Chord (m)	0.08	.09	0.10
Vertical Tail Span (m)	0.2	.28	.28
Vertical Tail Chord (m)	0.08	.08	.08
Tail Volume	0.494	1.04	1.07

## Full Configuration Parameters in Comparison

### I.1.9 Flight dynamics

Please refer to previous report for stability derivative for iteration 1 and 2. The stability derivative calculated from XFLR5 for iteration 3 is shown in Table.7 and Table.8. These stability derivatives for iteration 3 is not determined experimentally as the plane crashed before the trimming test.

**Table 7:** Longitudinal Stability Derivatives

	$V_{total} = 12.90885[m/s]$
$C_{xu}$	-0.079246
$C_{x\alpha}$	0.30083
$C_{zu}$	-0.0072312
$C_{za}$	-4.827
$C_{zq}$	-9.865
$C_{ma}$	-2.0279
$C_{mq}$	-28.741



**Table 8:** Lateral Stability Parameters

	$V_{total} = 12.90885[m/s]$
$C_{y\beta}$	-0.32804
$C_{lb}$	-0.036797
$C_{lp}$	-0.45741
$C_{lr}$	0.22073
$C_{nb}$	0.21805
$C_{np}$	-0.083761
$C_{nr}$	-0.31131

$C_{x\dot{\alpha}}$ ,  $C_{z\dot{\alpha}}$ ,  $C_{mu}$ ,  $C_{yp}$ ,  $C_{yr}$  for both planes were estimated to be 0, and  $C_{m\dot{\alpha}}$  was estimated as -3 as a typical value for conventional aircraft configuration.  $C_{y\phi} = \frac{mg}{Sq_\infty} \cos(\theta_0)$ ,  $C_{y\psi} = \frac{mg}{Sq_\infty} \sin(\theta_0)$ . These stability derivatives are plugged into longitudinal and later equation of motions shown below:

$$\begin{bmatrix} \frac{mU_0}{Sq_\infty} & -\frac{c}{2U_0}C_{x\dot{\alpha}} & 0 & 0 \\ 0 & \frac{mU_0}{Sq_\infty} - \frac{c}{2U_0}C_{z\dot{\alpha}} & 0 & 0 \\ 0 & -\frac{c}{2U_0}C_{m\dot{\alpha}} & \frac{I_{yy}}{Sq_\infty c} & 0 \\ 0 & 0 & 0 & 1 \end{bmatrix} \begin{bmatrix} \dot{u} \\ \dot{\alpha} \\ \dot{q} \\ \dot{\theta} \end{bmatrix} = \begin{bmatrix} C_{xu} & C_{x\alpha} & \frac{c}{2U_0}C_{xq} & C_w \cos(\theta_0) \\ C_{zu} & C_{z\alpha} & \frac{mU_0}{Sq_\infty} - \frac{c}{2U_0}C_{zq} & C_w \sin(\theta_0) \\ C_{mu} & C_{m\alpha} & \frac{c}{2U_0}C_{mq} & 0 \\ 0 & 0 & 1 & 0 \end{bmatrix} \begin{bmatrix} u \\ \alpha \\ q \\ \theta \end{bmatrix}$$

$$+ \begin{bmatrix} C_{x\delta_e} & C_{x\delta_T} \\ C_{z\delta_e} & C_{z\delta_T} \\ C_{m\delta_e} & C_{m\delta_T} \\ 0 & 0 \end{bmatrix} \begin{bmatrix} \delta_e \\ \delta_T \end{bmatrix}$$

$$\begin{bmatrix} \frac{mU_0}{Sq_\infty} & 0 & 0 & 0 & 0 \\ 0 & \frac{I_{xx}}{Sq_\infty b} & -\frac{I_{xz}}{Sq_\infty b} & 0 & 0 \\ 0 & -\frac{I_{xz}}{Sq_\infty b} & \frac{I_{zz}}{Sq_\infty b} & 0 & 0 \\ 0 & 0 & 0 & 1 & 0 \\ 0 & 0 & 0 & 0 & 1 \end{bmatrix} \begin{bmatrix} \dot{\beta} \\ \dot{p} \\ \dot{r} \\ \dot{\phi} \\ \dot{\psi} \end{bmatrix} = \begin{bmatrix} C_{y\beta} & \frac{b}{2U_0}C_{yp} & \frac{b}{2U_0}C_{yr} - \frac{mU_0}{Sq_\infty} & C_{y\phi} & C_{y\psi} \\ C_{l\beta} & \frac{b}{2U_0}C_{lp} & \frac{b}{2U_0}C_{lr} & 0 & 0 \\ C_{n\beta} & \frac{b}{2U_0}C_{np} & \frac{b}{2U_0}C_{nr} & 0 & 0 \\ 0 & 1 & 0 & 0 & 0 \\ 0 & 0 & 1 & 0 & 0 \end{bmatrix} \begin{bmatrix} \beta \\ p \\ r \\ \phi \\ \psi \end{bmatrix}$$

$$+ \begin{bmatrix} C_{y\delta_a} & C_{y\delta_r} \\ C_{l\delta_a} & C_{l\delta_r} \\ C_{n\delta_a} & C_{n\delta_r} \\ 0 & 0 \\ 0 & 0 \end{bmatrix} \begin{bmatrix} \delta_a \\ \delta_r \end{bmatrix}$$

The natural frequencies and damping ratios for all the dynamic mode are calculated by linearize the equation of motion into the following form,  $\dot{\vec{x}} = \mathbf{A}\vec{x} + \mathbf{B}\vec{u}$ , and then calculate the eigenvalue of the matrix  $\mathbf{A}$ . The natural frequencies and damping ratios for all the dynamic mode for trimmed speed  $V_{total} = 12.90885[m/s]$  are shown in Table 9 and Table 10.

**Table 9:** Longitudinal dynamic modes parameters

		$V_{total} = 12.90885[m/s]$
$\omega_{S.P.}$	short period mode natural frequency	$12.8 \frac{rad}{\tau}$
$\tau_{S.P.}$	short period mode time constant	0.142[s]
$\zeta_{S.P.}$	short period mode damping ratio	0.542
$\omega_{phugoid}$	phugoid mode natural frequency	$0.0484 \frac{rad}{\tau}$
$\tau_{phugoid}$	phugoid mode time constant	48.7[s]
$\zeta_{phugoid}$	phugoid mode damping ratio	0.424

**Table 10:** Lateral dynamic modes parameters

		$V_{total} = 12.90885[m/s]$
$\omega_{D.R.}$	Dutch roll mode natural frequency	$9.01 \frac{rad}{\tau}$
$\tau_{D.R.}$	Dutch roll mode time constant	0.471[s]
$\zeta_{D.R.}$	Dutch roll mode damping ratio	0.236
$\omega_{spiral}$	spiral mode natural frequency	$0.258 \frac{rad}{\tau}$
$\tau_{spiral}$	spiral mode time constant	-3.88[s]
$\zeta_{spiral}$	spiral mode damping ratio	-1
$\omega_{roll}$	roll mode natural frequency	$30.4 \frac{rad}{\tau}$
$\tau_{roll}$	roll mode time constant	0.0329[s]
$\zeta_{roll}$	roll mode damping ratio	1

Comparing to the previous configurations, the damping for all oscillatory modes all increased significantly. Although getting rid of the dihedral made the spiral divergence faster.

## I.2 Manufacturing

The wing of the final aircraft was made of foam with a circular carbon spar continuous along the entire span of the wing. The wing had no dihedral or taper which made this feasible. On the previous iteration, the wing tip dihedral had resulted in a discontinuous spar held

together with a wooden lock piece bonded inside each end of the hollow spar, but this broke multiple times prompting this design change.

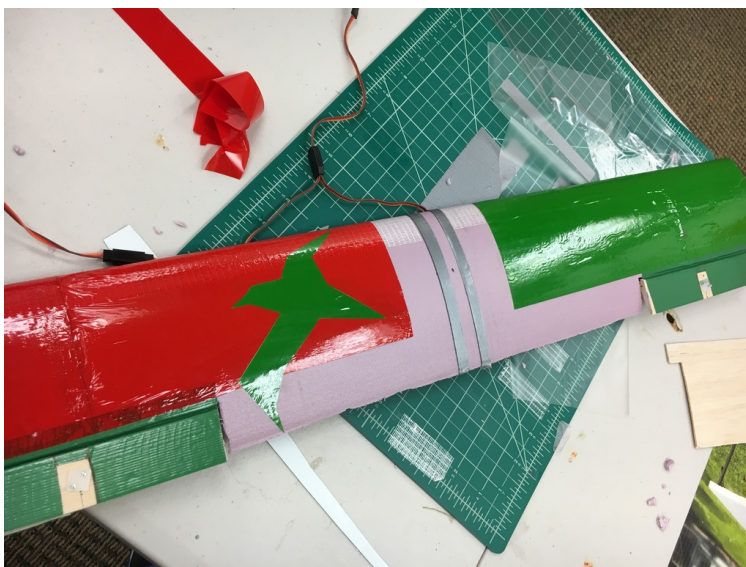


**Figure 11:** Albatross wing

To fasten the main wing to the fuselage, a wooden wing box was made with the laser cutter. This consisted of two wing profile cutouts close to the wing fuselage that encapsulate the wing and held it in place. The wing profile cutouts were split in half, leaving a top and bottom half of the wing box. This enabled us to remove the wing and/or replace the wing box without having to remake the other. This proved to be beneficial when our wing box broke multiple times with the wing still intact. To hold the wing inside the wing box, the wing cutout of the laser cut pieces was sized to be a press fit on the wing surface, and tape was placed on the wing surface just inside the wing box to constrain the wing laterally by not allowing the tape sections to fit through the wing box. The box was then Velcro'd to the fuselage and held down with rubber bands to securely fasten it.

To mount the tail, a portion of the vertical tail was bonded into the end of the carbon tube boom to provide a tail mount. The horizontal then slid inside a slot in the vertical tail sized exactly to the horizontal tail airfoil shape, and then the two were bonded together. To add strength, small wooden gussets were bonded between the vertical tail and spar of the horizontal tail. There was also a cutout in the vertical tail to save weight from the MDF wood we were using. We filled this hole with thin foam and covered it with a layer of tape. The vertical tail design proved to be flawed over time. In nearly every crash, the vertical tail section between the horizontal tail and carbon rod would fail and break off because it was too thin. We tried reinforcing it with both carbon strips and metal wire braces which

helped a small amount, but the tail still broke quite often and would need to be replaced. To keep the carbon tail boom from twisting in the fuselage, a small amount of epoxy was applied to the juncture of the fuselage and boom to secure it.

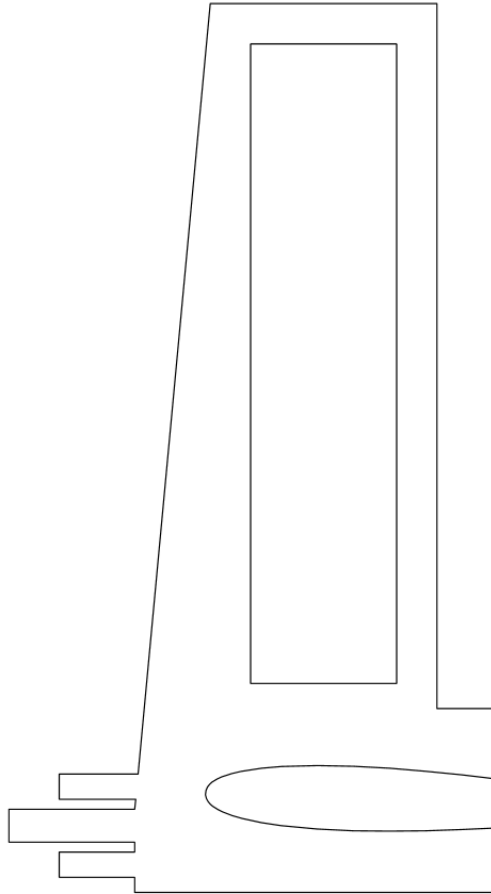


**Figure 12:** Vertical tail



**Figure 13:** Vertical and horizontal tail pieces

To fasten the main wing to the fuselage, a wooden wing box was made with the laser cutter. This consisted of three wing profile cutouts close to the wing fuselage that encapsulate the wing and hold it in place. The wing was glued inside the box, and the box then Velcro'd to the fuselage and held down with rubber bands to securely fasten it.

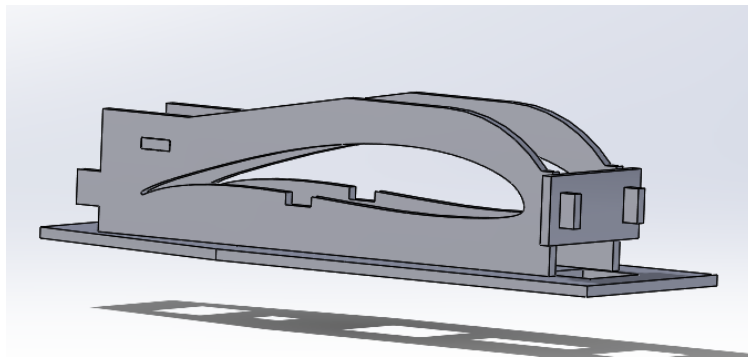


**Figure 14:** Wing mounting

Our control surfaces were made of balsa wood plates because we were unsure if the thin trailing edge of the foam would be stiff and sturdy enough to handle actuator inputs with

deforming or breaking. The ailerons were sized to be about a quarter of the span and a quarter of the chord. The elevator was sized to be 30 percent of the horizontal tail chord and across the entire span. The rudder was basswood and spanned the whole vertical tail except for a small section cut off at the bottom to avoid interference with the elevator. The servos for the ailerons were partially embedded inside the wing, while the elevator and rudder servos were placed inside the fuselage with a push rod reaching to the tail.



**Figure 15:** Albatross 3

## II Controls and Planning

The given mission for the 2017 AA241x class was to have the aircraft autonomously visit plume locations. In each of the 3 phases of the mission, 3-5 locations (and radii) would be given to the controller. The plane would then need to navigate to as many of the locations as possible before the 30 second phase was over.

This task requires multiple levels of control. First, a low level controller is necessary to

stabilize the plane in flight, holding velocity, roll angle and pitch angle to desired values. On top of this, a line following controller can command roll and pitch values to keep the plane following a line at constant altitude. Finally, a high level path planner must use the lower level logic in a sequence which guides the plane through the plume locations. In the following section, we discuss the implementation of our final control system design.

## II.1 Low Level Control System Design

The low level control on Albatross used successive loop closure for both longitudinal and lateral autopilot, which is the same technique used and tested on the Bixler. As shown in the stability analysis in Section I.1.9, the Albatross have faster natural frequency in all dynamic modes, and is more sensitive to control input than the Bixler. Due to limited time and unexpected crashes of the Albatross, we didn't have a lot of chance to fine tune the gains on the Albatross, but we lowered the gains that were used successfully on the Bixler during the mission on Monday Jun. 12th. This will be discussed later in this section and the gains are shown in Table.11. Section II.1.1 and Section II.1.2 will address update we made to our longitudinal and lateral autopilot.

### II.1.1 Longitudinal Autopilot

Based on previous result, we always have an offset between actual speed and the commanded speed, which can jeopardize the plane's performance when it's not flying at the designed speed. Therefore, we added a integrator gain to the throttle loop to reduce the steady state error. The new control diagram is shown in Fig.16. Note a 0-1 saturator is placed for the throttle servo to avoid and integrator wind-up issue. The code used Euler's method to do numerical integration.

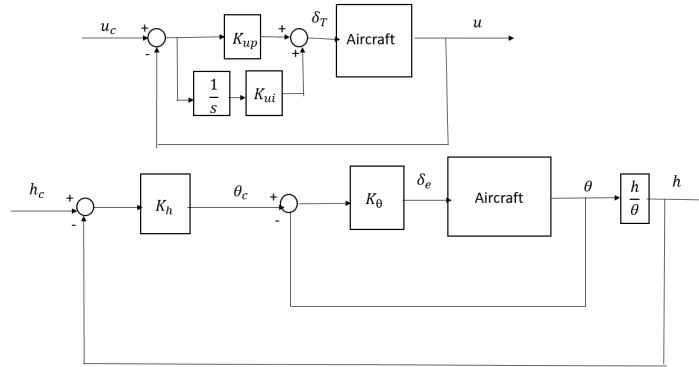


**Figure 16:** Longitudinal control loop

Now,  $\delta_T = K_{up}(u_c - u) + K_{ui}\frac{u_c - u}{s}$ . The control for the elevator stayed the same,  $\delta_e = K_\theta(\theta_c - \theta)$ . Experimentally, since  $K_{ui}$  used is very small, the effect of adding the integrator control is not very significant.

### II.1.2 Lateral Autopilot

The logic for lateral control is the same, as shown in Fig.17.

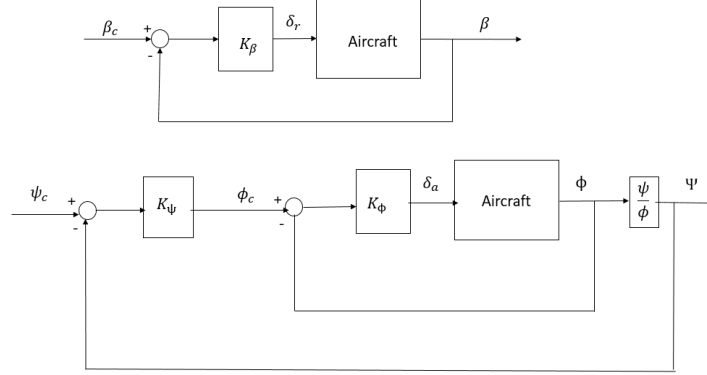


**Figure 17:** Lateral control loop

For coordinated turn, the rudder servo input is  $\delta_r = K_\beta(\beta_c - \beta)$ . The desired roll angle is calculated from error in yaw,  $\phi_c = K_\psi(\psi_c - \psi)$ , then the aileron servo output is still  $\delta_a = K_\phi(\phi_c - \phi)$ .

The  $\psi_c$  (desired course angle) input comes from the waypoint following logic. First, a desired path to follow is identified, starting from a point with position vector  $\mathbf{q}$ , and the angle that path makes with due north is computed as  $\chi_q$ . The plane's current position is denoted by  $\mathbf{p}$ . Then,

$$\begin{aligned} \mathbf{e} &= \mathbf{p} - \mathbf{q} \\ e_\perp &= \mathbf{e}_e \cos(\chi_q) - \mathbf{e}_n \sin(\chi_q) \\ \psi_c = \chi^c &= \chi_q - \chi_\infty \frac{2}{\pi} \arctan(k_{\text{path}} e_\perp) \end{aligned}$$

$\chi_\infty$  is a fixed approach angle chosen indicating how aggressive the plane tends to approach the line desired. Experimentally,  $\chi_\infty = \frac{\pi}{3}$  (more aggressive than the  $\chi_\infty = \frac{\pi}{5}$  started with) to achieve smaller turning radius.

For the mission, the paths to follow is simply the line connection between each plume location in the optimized order.



In implementing these control laws, we take care to wrap any computed angle errors to within  $[-\pi, \pi]$ , to ensure that the system corrects in the direction that requires the least effort.

### II.1.3 Control Parameters

The gains used experimentally for both the Bixler and the Albatross are shown in Table 11.

**Table 11:** Proportional controller gains

	Bixler	Albatross
$K_{up}$	0.821	0.821
$K_\beta$	-0.01	-0.01
$K_\psi$	0.250	0.250
$K_h$	0.032	0.032
$K_\theta$	3.00	1.00
$K_\phi$	3.00	2.00
$k_{path}$	0.05	0.05

The control gains used on Albatross is generally smaller than the ones used on the Bixler, however, during the mission on Jun 12th,  $K_\phi = 2.00$  still proved to be too big as visible roll oscillation was observed, which indicate roll correction overshoot.  $K_\phi$  should be further lowered if given the chance for more fly testing.

## II.2 Path Planning

Given a control system for following arbitrary line segments at a given altitude, to successfully complete the mission, we need a method to connect the plume locations in the mission into a single path that the plane can follow. This is the problem of selecting the optimum sequence of waypoints.

Given that the maximum number of waypoints in a given mission phase is 5, the number of permutations of the waypoints ( $5! = 120$ ) is not prohibitively large for a brute-force comparison of the sequences. We define a cost function for a given sequence of waypoints that is simply the sum of the turning angles between one segment to the next. In this way, the sequence requiring the fewest loops is selected.

### III Results and Analysis

#### III.1 Bixler Mission Test

The Bixler attempted the mission on Friday June 9th, 2017. We flew the mission with seed = 10. Figure 18 shows the trajectory for each of the three phases of the mission. We see that the Bixler was able to hit 7 out of the 12 targets.

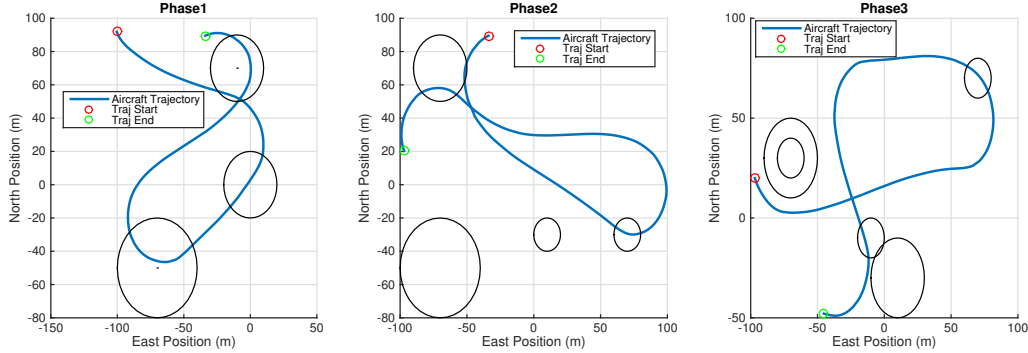


**Figure 18:** Trajectory of Bixler in the mission.

We see that in phase 3, a primary reason for mission the targets was the large turn radius under this controller. We attempted tuning the gains for this part of the controller somewhat in test flights but were unable to do all the tuning we desired due to limited time.

In phase 2, It seems that a poor choice of waypoint order caused the Bixler to have not enough time to visit all the waypoints. We discovered a bug in the C++ implementation of the path planning algorithm that meant that the turn angle heuristic was not being minimized, but maximized in one direction, but we were not able to fly a mission with the corrected code.

Figure 19 shows how course and altitude were tracked during the mission. We flew the mission at an altitude of 70m, and had the autopilot command an altitude of 50m at the end of the mission so that we could easily tell if the mission was finished. The course tracking was better than in our last waypoint navigation attempt, but still had room for improvement.

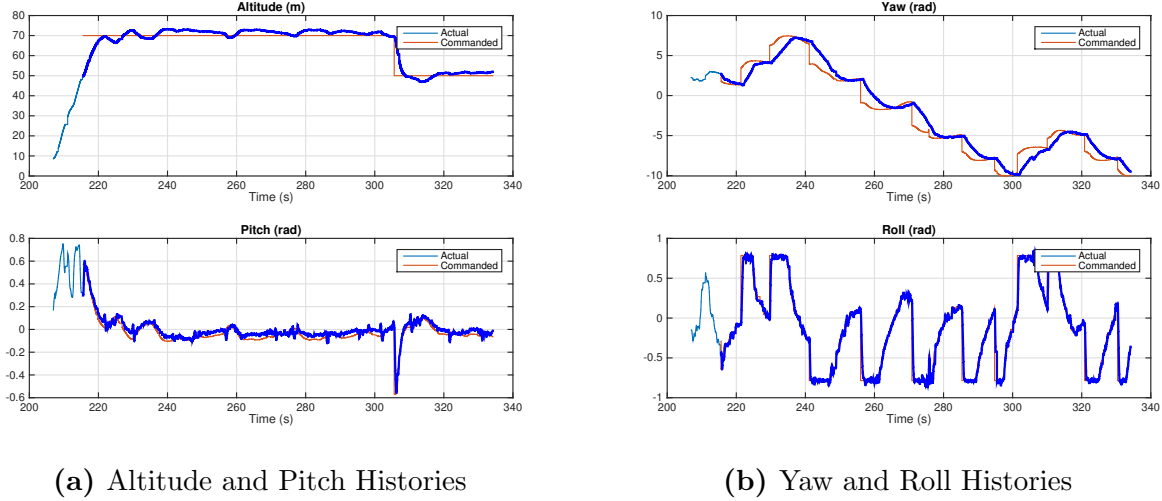


**Figure 19:** Altitude, Pitch, Course, and Roll histories during the Bixler’s mission.

### III.2 Albatross Mission Test

The Albatross 3 attempted the mission on Monday June 12th, 2017. The repaired version of the plane had never been flown before due to several crashes on the preceding Thursday that required repairs to the fuselage and tail. The plane was not tested over the weekend before the mission day for fear of another crash and having to make more repairs.

The four previous flights with the Albatross 3 had all resulted in rather quick failures (two on takeoff, one from loss of orientation, and one from having the aileron directions reversed when switching into mission mode), so none of our control gains had been tuned yet for this plane. We were confident in our mission code having tested it several times successfully on the Bixler, but were admittedly nervous about the performance of our plane.

At the start of the mission, the takeoff was okay. It didn’t crash to the ground, but it had a tendency to want to roll to the right and the pilot had trouble manually keeping it from dropping in altitude. To prevent the plane from crashing, it was switched into mission mode so the controller could hopefully handle the flight dynamics better, and it did. The plane gained altitude and set off for the other side of Lake Lagunita to fly the mission. Unfortunately, the altitude when mission mode was activated was too low, so the mission hadn’t officially begun. The plane went to the other side of the lake and then turned back, heading towards the Elliot Center. The plane kept a constant heading and was just about to fly past the lake and over our heads. Having heard that the mission was not active and being unsure of what the plane was then doing, the pilot switched it back into manual mode, when it then veered hard right towards the center of campus. The pilot should have switched it back into mission mode, but he panicked and tried to steer it back towards

the lake, unfortunately unsuccessfully. The plane continued to drift out over campus while continuously losing altitude until it eventually dropped out of sight. We were fortunate that it had apparently crashed into a tree and then a sidewalk without harming anyone. The crash damage was a broken wing box, broken telemetry antennae, broken rearmost fuselage piece, and a broken vertical tail. An attempt to repair the plane was made so that we could try to complete the mission, but the structural integrity of the tail was not sound enough to safely fly again, thus ending our day.

Our plane had been struggling with roll stability for several weeks now and we were unable to find a solution to the problem. One hypothesis is that our center of gravity was too high (from having a pretty highly mounted wing plus the pixhawk electronics) and so rolling to one side would cause that side to tip over even more. Our wing had no dihedral for roll stability and the wing box on top made the stability component of our high wing much less effective.

## Appendix

**Table 12:** Writing Contribution

Section	Name
I.1.1-I.1.7	Zhe Zhang
I.1.8	Victoria M Dax
I.1.9	Miao Zhang
I.2	Justin Schneider
II.1	Miao Zhang
II.2	Apoorva Sharma
III	Apoorva Sharma

## References

- [1] John H. Blakelock, *Automatic Control of Aircraft and Missile* A Wiley-Interscience publication: John Wiley & Sons, 1991.
- [2] Randal W. Beard, Timothy W. McLain, *Small Unmanned Aircraft: Theory and Practice*. Princeton University Press, 2012.